JOURNAL OF COMPUTATIONAL PHYSICS 71, 124–146 (1987)

NOVA: A Nonvariational Code for Solving the MHD Stability of Axisymmetric Toroidal Plasmas

C. Z. CHENG AND M. S. CHANCE

Princeton Plasma Physics Laboratory, Princeton, New Jersey 08544

Received March 21, 1986; revised September 29, 1986

A nonvariational approach for determining the ideal MHD stability of axisymmetric toroidal confinement systems is presented. The code (NOVA) employs cubic B-spline finite elements and Fourier expansion in a general flux coordinate (ψ, θ, ζ) system. At least as much accuracy and faster convergence were obtained in comparison with the existing variational PEST and ERATO codes which employ linear finite elements. This nonvariational approach benchmarked here on the ideal MHD problem is a prelude to a future extended version applicable to problems having non-Hermitian eigenmode equations where variational energy principles cannot be obtained. © 1987 Academic Press, Inc.

I. INTRODUCTION

Linear stability stability analysis of magnetohydrodynamic (MHD) modes in axisymmetric toroidal plasmas is crucial to thermonuclear fusion research. In particular, ideal MHD instabilities are thought to play an important role in limiting the β-values of tokamak devices. The mathematical problem is to solve the two-dimensional eigenmode equations and obtain the growth rates of the MHD instabilities. The exact solutions are impossible to obtain without the use of numerical computations. A number of two-dimensional normal mode codes [1–6] have been developed extensively to study the dependence of ideal MHD instabilities on a variety of parameters relating to the the geometry as well as the pressure and current profiles. As practical tools, they are used to aid in the design of new experiments and in the analysis of experimental data. All these ideal MHD codes utilize a Lagrangian formalism [7] for linearized perturbations and involve the use of the linear Galerkin procedure, which reduces the problem to the minimization of an algebraic quadratic form with respect to a certain set of variational parameters. The variational calculation is then reduced to the determination of eigenvalues and eigenfunctions of the matrix eigenvalue problem. Nonetheless, these codes have inherent limitations in their applications to various ideal MHD stability calculation and in their extensions to the nonideal MHD stability calculations. With the PEST code [1], for example, the choice of representation of the displacement vector prevents the stability analysis of equilibria where the toroidal field vanishes in plasmas, such as in the spheromak and reversed field pinch configurations. The PEST-2 [6], which is basically a numerical treatment of the energy principle, has

0021-9991/87 $3.00

eliminated this restriction, but has a major shortcoming in that it does not calculate the real physical growth rates or eigenfunctions of the ideal MHD instabilities. In addition, an important limitation of these codes is that because of their variational nature, they cannot be extended to the stability calculations of non-Hermitian eigenmode equations, such as in the cases of ideal MHD with equilibrium flows, resistive MHD and kinetic MHD etc., where variational energy principles cannot be established.

In this paper, we present a numerical method for integrating ideal MHD equations which can be easily generalized to integrate non-Hermitian eigenmode equations. The code (NOVA) does not involve variational energy principles. All these variational ideal MHD stability codes employed linear finite elements in the minor radius direction, which are the lowest order finite elements allowed for representing the displacement vector ξ. Since they are in quadratic forms, the numerical errors in the eigenvalues, ω^2, scale as N^{-2}, where N is the total number of the radial computational grid points. Therefore, our nonvariational approach requires higher order finite elements to achieve better accuracy and faster convergence. For example, with the cubic B-spline finite elements [8] the errors in ω^2 scale as N^{-4}. In a general flux coordinate (ψ, θ, ζ) system with an arbitrary Jacobian, the NOVA code employs Fourier expansion in the poloidal angle θ, as in the PEST code, and the cubic B-spline finite elements in the radial coordinate, ψ direction. An arbitrary nonuniform ψ-mesh, which still maintains the N^{-4} convergence property, is set up to provide the option of zoning the mesh to allow more finite elements near rational surfaces, the plasma edge, and the magnetic axis. In comparison with these existing variational ideal MHD stability codes, the NOVA code is at least as fast and accurate. However, if the existing variational ideal MHD stability codes are upgraded to employ higher order finite elements, they may be equally or more efficient than the NOVA code.

In the following, we first briefly describe in Section II the MHD equilibrium and present a class of generalized toroidal coordinate system which can greatly improve the representation of various MHD instabilities. In Section III, we present the ideal MHD eigenmode equations [9] and the corresponding boundary conditions for our nonvariational treatment. The numerical methods used to solve the eigenmode equations are described in Section IV. Convergence studies of the NOVA code are presented for the analytical Solovév equilibrium [10], and detailed comparisons, as presented with other variational codes [11], are given in Section V. Several applications of the NOVA code to numerical tokamak equilibria have indicated the accuracy and efficiency of this method, and are described in Section VI. In Section VII, we summarize the principal conclusions of this work.

II. Toroidal MHD Equilibrium and Flux Coordinate System

We consider stationary ideal MHD equilibria statisfying

$$\mathbf{J} \times \mathbf{B} = \nabla P, \qquad \nabla \times \mathbf{B} = \mathbf{J}, \qquad \text{and} \qquad \nabla \cdot \mathbf{B} = 0, \tag{1}$$

where **J**, **B**, and P are the equilibrium current density, magnetic field, and pressure, respectively. In terms of the flux coordinate system (ψ, θ, ζ), the equilibrium magnetic field with nested magnetic surfaces can be written as

$$\mathbf{B} = \nabla\zeta \times \nabla\psi + q(\psi)\,\nabla\psi \times \nabla\theta, \tag{2}$$

where $2\pi\psi$ is the poloidal flux within a magnetic surface, $q(\psi)$ is the safety factor, θ is the generalized poloidal angle varying between 0 and 2π, and ζ the generalized toroidal angle varying between 0 and 2π. Since

$$\mathbf{B}\cdot\nabla = \mathscr{J}^{-1}\left(\frac{\partial}{\partial\theta} + q\frac{\partial}{\partial\zeta}\right), \tag{3}$$

where the Jacobian $\mathscr{J}$ is defined by

$$\mathscr{J}^{-1} = \nabla\psi \times \nabla\theta \cdot \nabla\zeta, \tag{4}$$

the magnetic field lines are straight in this coordinate system.

For axisymmetric equilibria, we can also express the equilibrium magnetic field as

$$\mathbf{B} = \nabla\phi \times \nabla\psi + g(\psi)\,\nabla\phi, \tag{5}$$

where ϕ is the toroidal angle in the usual cylindrical coordinate (X, ϕ, Z) system. Then ψ can be determined numerically by solving the Grad–Shafranov equation,

$$\Delta^*\psi \equiv X^2\nabla\cdot\left(\frac{1}{X^2}\nabla\psi\right) = -(X^2P' + gg'), \tag{6}$$

if $P(\psi)$ and $g(\psi)$ are specified. Here, the prime denotes the partial derivative with respect to ψ. We can write the generalized toroidal angle ζ as

$$\zeta = \phi - q\delta(\theta, \psi), \tag{7}$$

where $\delta(\theta, \psi)$ is periodic in θ. Then from Eqs. (2) and (5), δ and $\mathscr{J}$ are related by

$$q\left(1 + \frac{\partial\delta}{\partial\theta}\right) = \frac{g\mathscr{J}}{X^2}. \tag{8}$$

Along a flux surface in the poloidal plane we have

$$\frac{ds}{d\theta} = \frac{\mathscr{J}\,|\nabla\psi|}{X}, \tag{9}$$

where ds is the element of arc length along a constant (ϕ, ψ) line. Specification of $\mathscr{J}$

therefore determines the θ coordinate. In this paper, we choose the Jacobian in the form

$$\mathcal{J}(X, Z) = \frac{X^i}{\alpha(\psi)|\nabla\psi|^j B^k}, \tag{10}$$

where i, j, k can be freely specified and $\alpha(\psi)$ is given by the requirement that θ increases by 2π during one poloidal circuit. The form of $\mathcal{J}$ in Eq. (10) is a trivial generalization of that used in the PEST-2 code [6]. Thus, from Eq. (9) we have

$$\alpha(\psi) = \frac{2}{\oint ds(|\nabla\psi|^{j-1}B^k/X^{i-1})}. \tag{11}$$

For the choice $i=2$, $j=k=0$, the (ψ, θ, ζ) coordinate represents the PEST-1 coordinate. For $i=j=1$, $k=0$, we have the equal arc length coordinate system, and a Hamada-like coordinate system is obtained by letting $i=j=k=0$. The choice $i=j=0$, $k=2$ is used in the Hamiltonian representation of the magnetic field [12].

The general flux coordinate system (ψ, θ, ζ) constructed here is not orthogonal and its metric is complicated because $\nabla\psi\cdot\nabla\zeta\neq 0$, $\nabla\theta\cdot\nabla\zeta\neq 0$, $\nabla\theta\cdot\nabla\psi\neq 0$, and $|\nabla\zeta|^2\neq 1/X^2$. However, ζ is still an ignorable coordinate for axisymmetric equilibria, and the perturbed quantities can be represented by a single mode varying as $\exp(-in\zeta)$.

III. Linearized Ideal MHD Eigenmode Equations

Let $\boldsymbol{\xi}$, $\mathbf{b}$, p_1 be the perturbed quantities for the plasma displacement, magnetic field, and plasma pressure, respectively. Taking the time dependence $\boldsymbol{\xi}(\mathbf{x}, t)=\boldsymbol{\xi}(\mathbf{x})\exp(-i\omega t)$ and applying the Laplace transform, the linearized ideal MHD equations governing the asymptotic behaviors of the perturbed quantities are given by

$$p_1 + \boldsymbol{\xi}\cdot\nabla P + \gamma_s P\nabla\cdot\boldsymbol{\xi} = 0, \tag{12}$$

$$\rho\omega^2\boldsymbol{\xi} = \nabla p_1 + \mathbf{b}\times(\nabla\times\mathbf{B}) + \mathbf{B}\times(\nabla\times\boldsymbol{b}), \tag{13}$$

and

$$\mathbf{b} = \nabla\times(\boldsymbol{\xi}\times\mathbf{B}), \tag{14}$$

where $\gamma_s = \frac{5}{3}$ is the ratio of specific heats, ρ is the plasma equilibrium density, and the initial source perturbations have been neglected because we are not interested in the transient phenomena. We decompose the displacement vector and perturbed magnetic field as

$$\boldsymbol{\xi} = \frac{\xi_\psi}{|\nabla\psi|^2}\nabla\psi + \frac{\xi_s}{B^2}(\mathbf{B}\times\nabla\psi) + \frac{\xi_b}{B^2}\mathbf{B} \tag{15}$$

and

$$\mathbf{b} = \frac{Q_\psi}{|\nabla\psi|^2}\nabla\psi + \frac{Q_s}{|\nabla\psi|^2}(\mathbf{B}\times\nabla\psi) + \frac{Q_b}{B^2}\mathbf{B}, \tag{16}$$

so that

$$\xi_\psi = \xi\cdot\nabla\psi, \qquad \xi_s = \xi\cdot\left(\frac{\mathbf{B}\times\nabla\psi}{|\nabla\psi|^2}\right), \qquad \xi_b = \xi\cdot\mathbf{B}, \qquad Q_\psi = \mathbf{b}\cdot\nabla\psi,$$

$$Q_s = \mathbf{b}\cdot\frac{(\mathbf{B}\times\nabla\psi)}{B^2}, \qquad \text{and} \qquad Q_b = \mathbf{b}\cdot\mathbf{B}.$$

The three components of the momentum equation, Eq. (13), obtained after taking the scalar products with $\nabla\psi$, $\mathbf{B}\times\nabla\psi$, and $\mathbf{B}$, can be rewritten as

$$\nabla\psi\cdot\nabla P_1 = \omega^2\rho\xi_\psi + |\nabla\psi|^2\,\mathbf{B}\cdot\nabla\left(\frac{\mathbf{B}\cdot\nabla\xi_\psi}{|\nabla\psi|^2}\right)$$
$$+ (|\nabla\psi|^2 S - \mathbf{B}\cdot\mathbf{J})\frac{|\nabla\psi|^2}{B^2}(\mathbf{B}\cdot\nabla\xi_s - S\xi_\psi) + 2\mathbf{K}\cdot\nabla\psi Q_b, \tag{17}$$

$$(\mathbf{B}\times\nabla\psi)\cdot\nabla P_1 = \omega^2\rho|\nabla\psi|^2\,\xi_s + (\mathbf{B}\cdot\mathbf{J})\,\mathbf{B}\cdot\nabla\xi_\psi$$
$$+ B^2\mathbf{B}\cdot\nabla\left[\frac{|\nabla\psi|^2}{B^2}(\mathbf{B}\cdot\nabla\xi_s - S\xi_\psi)\right] + 2\mathbf{K}\cdot(\mathbf{B}\times\nabla\psi)\,Q_b, \tag{18}$$

and

$$\omega^2\rho\xi_b = \mathbf{B}\cdot\nabla(p_1 + P'\xi_\psi), \tag{19}$$

where $P_1 = p_1 + \mathbf{b}\cdot\mathbf{B}$ is the total perturbed pressure, $P' = \partial P/\partial\psi$, $\mathbf{K} = (\mathbf{B}/B)\cdot\nabla(\mathbf{B}/B)$ is the magnetic field curvature, and $S = (\mathbf{B}\times\nabla\psi/|\nabla\psi|^2)\cdot\nabla\times(\mathbf{B}\times\nabla\psi/|\nabla\psi|^2)$ is the negative local magnetic shear. Similarly, the three components of the induction equation, Eq. (14), can be written as

$$Q_\psi = \boldsymbol{B}\cdot\nabla\xi_\psi, \tag{20}$$

$$Q_s = \left(\frac{|\nabla\psi|}{B}\right)^2(\mathbf{B}\cdot\nabla\xi_s - S\xi_\psi), \tag{21}$$

$$Q_b = B^2\mathbf{B}\cdot\nabla\left(\frac{\xi_b}{B^2}\right) - B^2\nabla\cdot\xi - 2\mathbf{K}\cdot(\mathbf{B}\times\nabla\psi)\,\xi_s$$
$$- 2\,(\mathbf{K}\cdot\nabla\psi)\frac{B^2}{|\nabla\psi|^2}\xi_\psi + P'\xi_\psi, \tag{22}$$

and $\nabla\cdot\xi$ can be explicitly expressed as

$$\nabla\cdot\xi=\frac{\nabla\psi\cdot\nabla\xi_\psi}{|\nabla\psi|^2}+\left[\nabla\cdot\left(\frac{\nabla\psi}{|\nabla\psi|^2}\right)\right]\xi_\psi+\frac{\mathbf{B}\times\nabla\psi\cdot\nabla\xi_s}{B^2}-2\mathbf{K}\cdot(\mathbf{B}\times\nabla\psi)\,\xi_s$$
$$+\mathbf{B}\cdot\nabla\left(\frac{\xi_b}{B^2}\right). \tag{23}$$

Now ξ_b, Q_ψ, Q_s, and Q_b can be eliminated by using Eqs. (19)–(22) and from Eqs. (12), (17), (18), and (23) the linearized ideal MHD eigenmode equation can be cast into the form [9]

$$\nabla\psi\cdot\nabla\begin{pmatrix}P_1\\ \xi_\psi\end{pmatrix}=C\begin{pmatrix}P_1\\ \xi_\psi\end{pmatrix}+D\begin{pmatrix}\xi_s\\ \nabla\cdot\xi\end{pmatrix} \tag{24}$$

and

$$E\begin{pmatrix}\xi_s\\ \nabla\cdot\xi\end{pmatrix}=F\begin{pmatrix}P_1\\ \xi_\psi\end{pmatrix}, \tag{25}$$

where C, D, E, F are 2×2 matrix operators involving only surface derivatives $\mathbf{B}\cdot\nabla$ and $(\mathbf{B}\times\nabla\psi)\cdot\nabla$. The matrix operators are given by

$$C=\begin{pmatrix}2K_\psi & G\\ 0 & -|\nabla\psi|^2\nabla\cdot\left(\dfrac{\nabla\psi}{|\nabla\psi|^2}\right)\end{pmatrix}, \tag{26}$$

$$D=\begin{pmatrix}(|\nabla\psi|^2S-\mathbf{B}\cdot\mathbf{J})\dfrac{|\nabla\psi|^2}{B^2}\mathbf{B}\cdot\nabla & 2\gamma_sPK_\psi\\ |\nabla\psi|^2\left(2K_s-\dfrac{\mathbf{B}\times\nabla\psi}{B^2}\cdot\nabla\right) & |\nabla\psi|^2\left[1+\dfrac{\gamma_sP}{\omega^2\rho}\mathbf{B}\cdot\nabla\left(\dfrac{\mathbf{B}\cdot\nabla}{B^2}\right)\right]\end{pmatrix}, \tag{27}$$

$$E=\begin{pmatrix}\dfrac{\omega^2\rho|\nabla\psi|^2}{B^2}+\mathbf{B}\cdot\nabla\left(\dfrac{|\nabla\psi|^2\,\mathbf{B}\cdot\nabla}{B^2}\right) & 2\gamma_sPK_s\\ 2K_s & \dfrac{\gamma_sP+B^2}{B^2}+\dfrac{\gamma_sP}{\omega^2\rho}\mathbf{B}\cdot\nabla\left(\dfrac{\mathbf{B}\cdot\nabla}{B^2}\right)\end{pmatrix}, \tag{28}$$

$$F=\begin{pmatrix}-2K_s+\dfrac{\mathbf{B}\times\nabla\psi}{B^2}\cdot\nabla & \mathbf{B}\cdot\nabla\dfrac{|\nabla\psi|^2}{B^2}S-\dfrac{\mathbf{J}\cdot\mathbf{B}}{B^2}\mathbf{B}\cdot\nabla-2P'K_s\\ -\dfrac{1}{B^2} & \dfrac{-2K_\psi}{|\nabla\psi|^2}\end{pmatrix}, \tag{29}$$

where in Eqs. (26)–(29), $\mathbf{B}\cdot\nabla$ operates on all the quantities on its right side, and also note that in Eq. (24)–(29),

$$\nabla\psi\cdot\nabla = |\nabla\psi|^2\frac{\partial}{\partial\psi} + (\nabla\psi\cdot\nabla\theta)\frac{\partial}{\partial\theta} + (\nabla\psi\cdot\nabla\zeta)\frac{\partial}{\partial\zeta},$$

$$G = \omega^2\rho + 2P'K_\psi + |\nabla\psi|^2\,\mathbf{B}\cdot\nabla\left(\frac{\mathbf{B}\cdot\nabla}{|\nabla\psi|^2}\right) + (\mathbf{B}\cdot\mathbf{J} - S|\nabla\psi|^2)\frac{S|\nabla\psi|^2}{B^2},$$

$$K_\psi = \mathbf{K}\cdot\nabla\psi, \qquad \text{and} \qquad K_s = \mathbf{K}\cdot\frac{\mathbf{B}\times\nabla\psi}{B^2}.$$

The boundary condition at the magnetic axis is $\xi_\psi = 0$. For fixed boundary modes the boundary condition is $\xi_\psi = 0$ at the plasma-wall interface. For free boundary modes the boundary condition at the plasma-vacuum interface is given by $\mathbf{b}_v\cdot\nabla\psi = \mathbf{B}\cdot\nabla\xi_\psi$, where $\mathbf{b}_v$ is the vacuum magnetic field which must be solved from the divergence-free equation $\nabla\cdot\mathbf{b}_v = 0$.

For a given equilibrium we first solve ξ_s and $\nabla\cdot\xi$ in terms of P_1 and ξ_ψ from Eq. (25) by inverting the surface matrix operator E. Equation (24) then reduces to an equation for P_1 and ξ_ψ. Admissible regular solutions must be periodic in both θ and ζ, and satisfy the appropriate boundary conditions. This procedure fails if the inverse of the surface matrix operator E does not exist for a given ω at some ψ surface. Then only non-square-integrable solutions with spatial singularities at the singular surface are possible. If at each surface nontrivial single-valued periodic solutions in θ and ζ can be found for the equation

$$E\begin{pmatrix}\xi_s\\ \nabla\cdot\xi\end{pmatrix} = 0, \tag{30}$$

the corresponding set of eigenvalues ω^2 forms the continuous spectrum for the equilibrium [13, 14]. Equation (30) represents the coupling of the sound waves and the shear Alfvén waves through the surface component of the magnetic curvature and the plasma pressure. Equations (24) and (25) represent the toroidal generalization of the set of eigenmode equations derived by Appert *et al.*, [15] for the circular cylindrical pinch.

IV. Numerical Methods

The eigenmode equations, Eqs. (24) and (25), are solved by the Galerkin method, where the eigenfunction is represented by a linear superposition of a finite subset of a complete set of basis functions. We first represent the perturbed quantities by a finite Fourier series in θ,

$$\xi(\psi,\theta,\zeta) = \sum_m \xi_m(\psi)\exp[i(m\theta - n\zeta)], \tag{31}$$

where the summation over m is truncated to a total number of L poloidal harmonics, and n is the toroidal mode number. The equilibrium quantities are defined on M θ-points, where M is usually much larger than L. The elimination of ξ_s and $\nabla\cdot\xi$ proceeds by finding the algebraic Fourier matrix representation of the surface operators C, D, E, and F. Introducing the bracket notation,

$$E_{m'm} \equiv \langle m' |\, E \,| m \rangle \equiv \frac{1}{2\pi} \oint d\theta [\exp(-im'\theta)]\, E[\exp(im\theta)], \tag{32}$$

Eq. (25) reduces to

$$E_{m'm} \begin{pmatrix} \xi_s \\ \nabla\cdot\xi \end{pmatrix}_m = F_{m'm} \begin{pmatrix} P_1 \\ \xi_\psi \end{pmatrix}_m, \tag{33}$$

where the Fourier indices m' and m have the same truncated domain. Note that the evaluation of the algebraic matrix operations, $E_{m'm}$ etc., involves convolutions that occur in evaluating operator products and is done by employing FFT (Fast Fourier Transform). To avoid aliasing errors, a larger truncated Fourier series domain than L, say L^*, is imposed on $E_{m'm}$ and $F_{m'm}$ for inverting $E_{m'm}$ in Eq. (33). Now $E_{m'm}$ can be inverted to obtain ξ_{sm} and $(\nabla\cdot\xi)_m$ in terms of P_{1m} and $\xi_{\psi m}$, through a $(L^*\times L^*)$ matrix inversion. Note L^* is increased until the values of ξ_{sm} and $(\nabla\cdot\xi)_m$ are satisfactorily converged. Finally by eliminating P_{1m} in favor of $\xi_{\psi m}$, Eq. (24) is reduced to a set of L second-order differential equations.

$$\frac{\partial}{\partial r} H^{(1)}_{m'm} \frac{\partial}{\partial r} \xi_m + H^{(2)}_{m'm} \frac{\partial}{\partial r} \xi_m + H^{(3)}_{m'm} \xi_m + \frac{\partial}{\partial r} [H^{(4)}_{m'm} \xi_m] = 0, \tag{34}$$

where the H's are algebraic $L\times L$ matrices and are functions of r only, where $r = (\psi/\psi_{\text{tot}})^{1/2}$ and $\xi_m = \xi_{\psi m}/r$ is a vector of dimension L. The explicit expressions of the H's are too tedious and complicated to present in full detail here. The boundary conditions at the magnetic axis are now modified to $\xi_m = 0$ for $m^2 \neq 1$ and $\partial\xi_m/\partial r = 0$ for $m^2 = 1$.

We mention here that the MHD fast wave spectrum is best calculated numerically using the coupled sets of first order equations given by Eqs. (24) and (25), rather than the second order equation, Eq. (34), because of the apparent singularity in Eq. (34) related to those frequencies.

Equation (34) is integrated by employing cubic B-spline finite elements [8, 16] with the representation

$$\xi_m(r) = \sum_{k=1}^{N+2} \xi_{mk} U_k(r), \tag{35}$$

where the U's are the cubic B-spline finite elements, N is the total number of radial grid points, and we require $(N+2)$ cubic B-spline elements with $N \geqslant 5$. The cubic B-spline elements are localized piecewise cubic polynomials occupying four grid

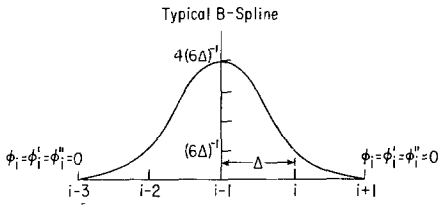

FIG. 1. Typical cubic B-spline finite element for a uniform grid.

intervals with continuity up to second derivatives, and are shown in Fig. 1. The errors in this representation scale as N^{-4} even for nonuniform grids [8]. Note that the cubic spline has the property of minimum curvature among all third order polynomials. For a detailed description of the cubic B-spline finite elements interested readers are referred to Ref. [8].

Now operating on Eq. (34) with the projection operator, $O_k = \int_0^1 dr\, U_k$, we obtain a set of algebraic equations

$$\sum_{m,k} M_{mk}^{m'k'} \xi_{mk} = 0, \tag{36}$$

where $M_{mk}^{m'k'}$ is an $(N+2)L \times (N+2)L$ matrix with nonvanishing elements along its L^2 7-banded diagonals. The errors associated with the Gibb's phenomena, which could be present when using higher order elements to represent functions containing regions with singular-like behavior, can be reduced by using an unequal grid spacing with packing near these regions. Because of the integral method employed here, the subsequent error in the matrix elements should be negligibly small when the projection operation is carried out. After imposing the boundary conditions to modify the matrix M, the nontrivial solution of Eq. (36) can be obtained by requiring

$$f(\omega^2) \equiv \det |M(\omega^2)| = 0. \tag{37}$$

The eigenvalue problem is therefore nonlinear in ω^2 and its numerical solution must be found by iteration. Convergence is assumed if $|[f(\omega_{p+1}^2) - f(\omega_p^2)]/f(\omega_p^2)| < \varepsilon_1$, and/or $|\omega_{p+1}^2 - \omega_p^2| < \varepsilon_2$, where ε_1 and ε_2 are appropriate small numbers, and p denotes the iteration step. When the eigenvalue iteration is converged to the required accuracy, Eq. (36) is used to construct the eigenvectors ξ and P_1. For this purpose, the matrices C, D, E, F for each surface are saved in disk files when they are computed during the calculation of the matrix elements of $M_{mk}^{m'k'}$. To make sure that the most unstable eigenvalue is obtained, we first locate all the unstable roots by evaluating $f(\omega^2)$ at ω_i^2 values over a large domain say $[\omega_1^2 \leqslant \omega_i^2 \leqslant \omega_2^2]$. If $f(\omega_1^2) f(\omega_2^2) < 0$, then there must be at least one root between ω_1^2 and ω_2^2. Usually ω_2^2 is decreased to a larger negative value to ensure a complete result. For the nonideal MHD problem, ω is usually complex and there are several ways to search for

the eigenvalue. One way is to employ the Cauchy theorem to search for the number of zeros of $f(\omega)$ over a certain complex ω-domain, although at the cost of greater computer time. When a zero is located in a certain ω-domain, a higher order complex root finder using the Muller method can be applied to obtain the converged eigenvalue efficiently.

The iteration is expensive computationally because the matrix inversion must be carried out for Eq. (33) at each iteration for each surface. Consequently, the execution times scale as the total number of radial grid points N as well as L^2 for the matrix inversion. Finally, to be consistent we have also employed the cubic B-spline finite elements to obtain the equilibrium quantities from the mapping codes.

Next, we consider the vacuum solution of $\nabla \cdot \mathbf{b}_v = 0$ with the vacuum region surrounded by a conducting wall. For $n \neq 0$ modes, we represent $\mathbf{b}_v = \nabla\chi$. Then in terms of the Green's theorem we have

$$2\pi\chi(\mathbf{x}_s) = \int d\mathbf{s}_t \cdot [G(\mathbf{x}_t | \mathbf{x}_s) \nabla_t \chi(\mathbf{x}_t) - \chi(\mathbf{x}_t) \nabla_t G(\mathbf{x}_t | \mathbf{x}_s)], \tag{38}$$

where we have chosen the Green's function G to satisfy

$$\nabla_t^2 G(\mathbf{x}_t | \mathbf{x}_s) = 4\pi\delta(\mathbf{x}_t - \mathbf{x}_s), \tag{39}$$

and $G(\mathbf{x}_t | \mathbf{x}_s) = |\mathbf{x}_t - \mathbf{x}_s|^{-1}$. Now $\mathbf{x}_s$ can be either on the plasma-vacuum interface or one the wall, and the integral extends over both surfaces in Eq. (38). With the boundary conditions $\nabla\chi \cdot \nabla\psi = \mathbf{B} \cdot \nabla\xi_\psi$ on the plasma-vacuum interface and $\nabla\chi \cdot d\mathbf{s}_w = 0$ on the wall, Eq. (38) can be solved to obtain χ on both surfaces by the method of collocation [17].

For the $n = 0$ mode, the magnetic field cannot be described by a single-valued scalar potential. Instead, we follow the precedure of Lüst and Martensen [18] and define

$$\mathbf{b}_v = \nabla\chi + a_1 \nabla\phi \times \nabla\alpha + a_2 \nabla\phi, \tag{40}$$

where a_1 and a_2 are constants related to the perturbed quantities. χ can be obtained by the same procedure as for $n \neq 0$ modes with the additional constraint $\oint \chi \, d\theta = 0$ due to the singular nature of the matrix in Eq. (38) for the $n = 0$ mode. α can be solved by taking $\nabla\phi \cdot \nabla \times \mathbf{b}_v = 0$ and we have [1]

$$\Delta^* \alpha \equiv \nabla \cdot \left(\frac{\nabla\alpha}{X^2} \right) = 0. \tag{41}$$

The boundary conditions are $\alpha = 1$ on the plasma-vacuum interface and $\alpha = 0$ on the wall. Equation (41) again can be solved using Green's theorem

$$\frac{4\pi^2 \alpha(\mathbf{x}_s)}{X_s} = \oint \frac{d\mathbf{s}_t}{X_t^2} \cdot [\hat{G}(\mathbf{x}_t | \mathbf{x}_s) \nabla_t \alpha(\mathbf{x}_t) - \alpha(\mathbf{x}_t) \nabla_t \hat{G}(\mathbf{x}_t | \mathbf{x}_s)], \tag{42}$$

where the Green's function $\hat{G}$ satisfies

$$\Delta_t^* \hat{G}(\mathbf{x}_t | \mathbf{x}_s) = -\frac{4\pi}{X_s^2} \delta(X_t - X_s)\, \delta(Z_t - Z_s), \tag{43}$$

and is given by

$$\hat{G}(\mathbf{x}_t | \mathbf{x}_s) = -\frac{4\pi X_t}{r} P^1_{-1/2}(w), \tag{44}$$

where $P^1_{-1/2}$ is the associated generalized Legendre function,

$$r = [(X_s^2 - X_t^2)^2 + (Z_s - Z_t)^4 + 2(X_s^2 + X_t^2)(Z_s - Z_t^2)]^{1/4} \tag{45}$$

and

$$w = \frac{[X_s^2 + X_t^2 + (Z_s - Z_t)^2]}{r^2}. \tag{46}$$

To determine a_1 and a_2 we make use of the property

$$\int \nabla\chi \cdot \nabla\phi \, d^3x = \int \nabla\chi \cdot (\nabla\phi \times \nabla\alpha)\, d^3x = 0.$$

Then, with the aid of the boundary conditions $\mathbf{A} \times d\mathbf{s}_w = 0$ on the wall and $\mathbf{A} \times \nabla\psi = \xi_\psi \mathbf{B}$ on the plasma-vacuum interface, where $\mathbf{A}$ is the vector potential defined by $\mathbf{b}_v = \nabla \times \mathbf{A}$, we obtain

$$a_1 = \frac{\oint (\nabla\phi \times \nabla\alpha) \cdot (\hat{n}_p \times \mathbf{A})\, ds_p}{\int |\nabla\phi \times \nabla\alpha|^2 \, d^3x} \tag{47}$$

and

$$a_2 = \frac{\oint \nabla\phi \cdot (\hat{n}_p \times \mathbf{A})\, ds_p}{\int |\nabla\phi|^2 \, d^3x}, \tag{48}$$

where s_p denotes the plasma surface and $\hat{n}_p = -\nabla\psi/|\nabla|$. After we solve the vacuum magnetic field $\mathbf{b}_v$ in terms of ξ_ψ, we obtain the boundary condition for solving Eqs. (24) and (25) at the plasma-vacuum interface

$$P_1 = \mathbf{b}_v \cdot \mathbf{B} = \sum_{m,m'} \tilde{M}_{mm'} \xi_{\psi m'} \exp[i(m\theta - n\zeta)]. \tag{49}$$

Note that P_1 is related to ξ_ψ and $\partial\xi_\psi/\partial\psi$ in Eq. (24).

This concludes our discussions on the vacuum solutions. For more details, the reader is referred to Ref. [17].

V. Convergence Studies

To illustrate the convergence properties of the code, we consider the analytic Solovév equilibria [10] which have been used previously [11] for extensive comparisons of variational ideal MHD stability codes. Our results will be compared with the previous results, which provide a series of cross checks essential for validating such a large, complex code. The Solovév equilibria which satisfy the Grad–Shafranov equation, Eq. (6), with $g' = 0$ are given by

$$\psi = \frac{\pi B_0}{ER^2 q(0)} \left[X^2 Z^2 + \frac{E^2}{4} (X^2 - R^2) \right], \tag{50}$$

$$P(\psi) = \frac{(1+E^2)\, B_0}{2\pi E R^2 q(0)} (\psi_B - \psi), \tag{51}$$

$$q(\psi) = RB_0 \oint \frac{ds}{X|\nabla\psi|}, \tag{52}$$

where (X, ϕ, Z) is a cylindrical coordinate system, B_0 is the toroidal field at the magnetic axis $X = R$, $P(\psi)$ is the plasma pressure, and $q(\psi)$ is the safety factor with the contour of integration along a line of constant ψ and ϕ. The system is characterized by the parameters: the ellipticity E, the inverse aspect ratio $\{\varepsilon \equiv [\psi_B q(0)/\pi E R^2 B_0]\}^{1,2}$ and $q(0)$. The wall position is specified by $\Lambda = (\psi_w/\psi_B)^{1,2}$, and $2\pi\psi_B$ is the total poloidal flux in the plasma.

To achieve the correct eigenvalue and an accurate representation of the corresponding eigenfunction, in principle one requires a very large number of basis expansion functions. Since this number is limited by the computer memory and

because the extrapolation formulas are simple.

Numerical convergence is shown below for the small aspect ratio, elliptical case with the parameters: $R = B_0 = 1$, $E = 2$, $\varepsilon = \frac{1}{3}$, $q(0) = 0.3$, $\Lambda = 1$, and $n = 2$. We employ a uniform r-mesh of N grid points and retain the poloidal harmonics $m = [-L_0, L_0]$. For the equal arc-length θ coordinate, the convergence curves of the eigenvalue ($\gamma^2 \equiv -\omega^2$) are shown in Fig. 2. Here γ^2 is normalized in terms of $B^2(0)/\rho(0)\, q^2(1)\, R^2$. The eigenvalue γ^2 scales as $\gamma^2 = \gamma_1^2 + C_1 \exp(-L_0/2)$ for fixed N and as $\gamma^2 = \gamma_2^2 + C_2 N^{-4}$ for fixed L_0, where γ_1^2 and γ_2^2 are the converged value for fixed N and L_0, respectively. The results from the PEST code show that γ^2 scales as $\gamma^2 = \gamma_3^2 + D_1 \exp(-L/2)$ for fixed N, where $L = 2L_0 + 1$, and for fixed L, as $\gamma^2 = \gamma_4^2 + D_2 B^{-2}$. Note that if we use the PEST θ-coordinate, the growth rate from our code also scales as $\gamma^2 = (\gamma_1^2 + \hat{C}_1 \exp(-L/2))$. Convergence curves from the PEST code are also shown in Fig. 2. Detailed comparison between the results of our code and those of the PEST code indicates that $|C_1| \sim |D_1|$ and $|C_2| \ll |D_2|$. Even with $N = 5$, our code converges in L_0 with an error of less than 1% of its converged value. On the other hand, comparable accuracy from the PEST code would

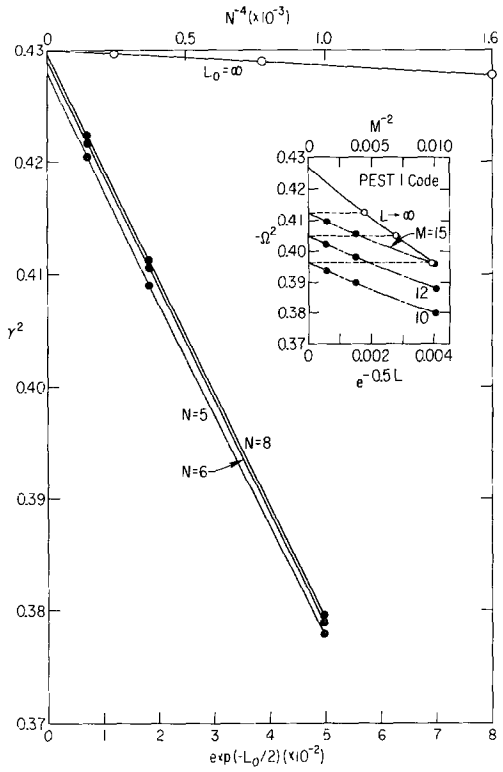

FIG. 2. Comparisons of convergence results in both the radial and the poloidal directions for our nonvariational code and the PEST code. The Solovev equilibrium has the parameters $R = B_0 = 1$, $E = 2$, $\varepsilon = \frac{1}{3}$, $q(0) = 0.3$, $A = 1$, and $n = 2$. The eigenvalue γ^2 is extrapolated numerically in both the number of poloidal harmonics and the number of radial finite elements.

TABLE I

Comparison of the Eigenvalues γ^2 for Different Solovév Equilibria from Various Ideal MHD Stability Codes

ε	E	A	$q(0)$	$q(a)$	n	Kerner	PEST-1	ERATO	Degtyarev	NOVA
$\frac{1}{6}$	1	2	1.791	2.0	1	0.202	0.204	—	0.211	0.208
$\frac{1}{6}$	1	2	2.2387	2.5	1	0.504	0.506	—	0.511	0.508
$\frac{1}{3}$	2	1	0.3	0.5224	2	0.413	0.427	0.431	0.430	0.430
$\frac{1}{3}$	2	1	0.7	1.219	2	0.118	0.119	0.120	0.121	0.119
$\frac{1}{3}$	2	∞	1.2	2.0897	1	—	0.75	0.78	—	0.748
$\frac{1}{3}$	2	∞	2.0	3.4829	1	—	0.68	0.75	—	0.656
$\frac{1}{3}$	2	∞	0.6	1.0449	2	—	1.31	1.40	1.32	1.35
$\frac{1}{3}$	2	∞	1.0	1.7415	2	—	1.03	1.07	1.06	1.038

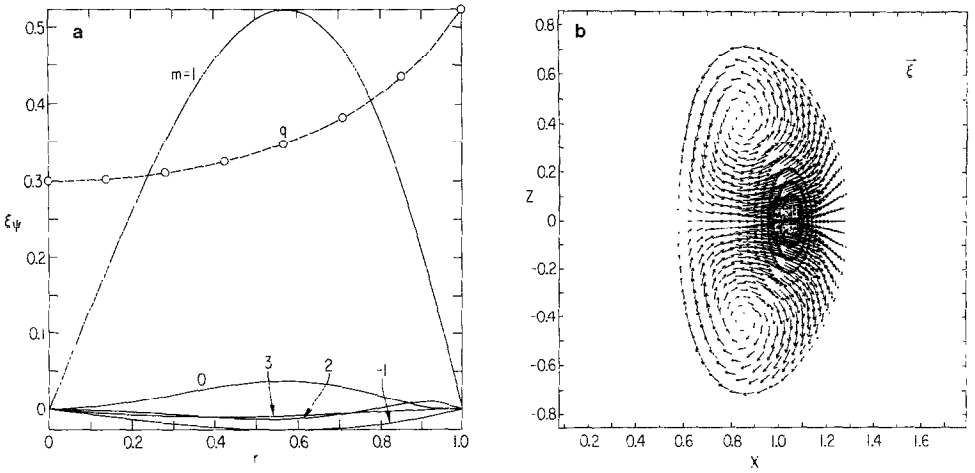

FIG. 3. (a) The poloidal harmonics of the eigenfunction ξ_ψ versus r and (b) the projection of the displacement vector onto the $\phi = 0$ plane for the converged solution as shown in Fig. 2. The q-profile is also shown in Fig. 3(a).

require at least three times as many linear finite elements. The eigenfunction ξ_ψ and the plasma flow pattern for this are shown in Figs. 3a and 3b, respectively. Comparisons of the converged values of the square of growth rates from different Solovév equilibria obtained from various ideal MHD stability codes [11] are summarized in Table I. For most of the cases, our results are roughly between those of PEST [1] and ERATO [2] codes. These small discrepancies may be due to different mapping codes used in these stability codes. We note that the difference in γ^2 for all stability codes are larger when vacuum solutions are required (i.e., $\lambda > 1$), which may be related to different methods of solving the vacuum problem in all stability codes.

VI. APPLICATIONS

In this section we present several test cases of calculating eigenvalues from numerical equilibria. NOVA can make use of an arbitrarily spaced radial mesh and has the opinion of rezoning this mesh to allow various nodes of the radial finite elements to coincide with the rational surfaces. Our experience in choosing various θ-coordinate systems does not warrant an optimal one. The best choice of θ may be determined by the requirements for an accurate and efficient calculation of the toroidal equilibrium quantities as well as accurate and efficient representation of the eigenfunction involved. Since these issues are problem dependent, the ability of choosing arbitrary Jacobian (or θ-coordinate) and arbitrary radial mesh is essential. It provides not only the extra confidence in the results which come from obtaining

consistent eigenvalues from different coordinate systems, but also the physical insight of the MHD perturbations. In general, because it distributes mesh points uniformly over the plasma surfaces, the equal arc-length θ-coordinate is usually a good choice. For a small aspect ratio bean-shaped tokamak where the PEST θ-coordinate does not sample the region on the outside of the torus very well, the equal arc-length system is indeed much superior. We have applied our code to study external kinks, internal kinks, toroidicity-induced global Alfvén modes, and the continuum modes for toroidal equilibria of various shapes and β values. The results are described below.

VI.a. *External Kink Modes*

The external kink instabilities are studied for a high-β bean-shaped equilibrium [19] with the plasma surface defined by $X = \tilde{X}_0 + \rho \cos \lambda$, $Z = E\rho \sin \lambda$, $\rho = A(1 + B \cos t)$, $\lambda = C \sin t$, with $\tilde{X}_0 = 2.71$, $E = 0.895$, $A = 1$, $B = 0.6$, and $C = 1.693$. This corresponds to $d/2a = 0.3035$, $b/a = 1.7385$, and $R/A = 3.449$, as shown in Fig. 4. The equilibrium profiles are defined by $P(y) = P_0(1.003 - y^2)^2$, and $q(y) = \sum_{i=0}^{3} q_i y^i$, where $y = \psi/\Delta\psi$, $P_0 = 0.109$, $q(0) = 1.03$, $q(1) = 4.2$, $q'(0) = 0.84375$, $q'(1) = 9.0$, and $\Delta\psi = 0.248$ is the plasma poloidal flux. The average beta is $\langle\beta\rangle = 8.75\%$. Note that q_i's are uniquely determined by $q'(0)$, $q(1)$, $q'(0)$, and $q'(1)$. The external kink mode has the eigenvalue $\gamma^2 = 3.5$ and has maximum amplitude near the plasma surface. Therefore an optimal radial coordinate is the uniform ψ-grid because it samples more grid points near the edge. The convergence in θ (i.e., Fourier harmonics) is much more rapid for the equal arc length θ-coordinate, because the PEST θ-grid concentrates more grid points around the tips of the beam, but the mode has more weight toward the outside of the torus. In fact, the equal arc length θ-coordinate is rapidly convergent with an error of less than 2% of its converged value with $-5 \leqslant m \leqslant 8$. Comparable accuracy with the PEST θ-coordinate would require approximately three times as many Fourier components for the positive maximum m, i.e., $-5 \leqslant m \leqslant 25$. These results are obtained by our NOVA code and can be clearly seen in Figs. 5 and 6 which show the poloidal com-

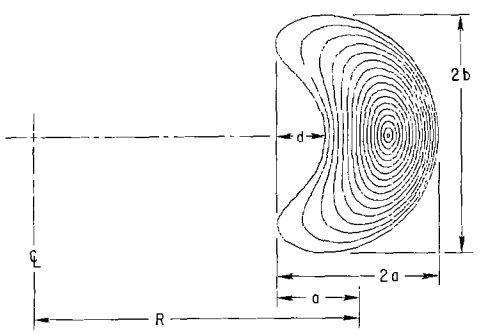

FIG. 4. The flux surface of a typical high-β bean-shaped tokamak equilibrium.

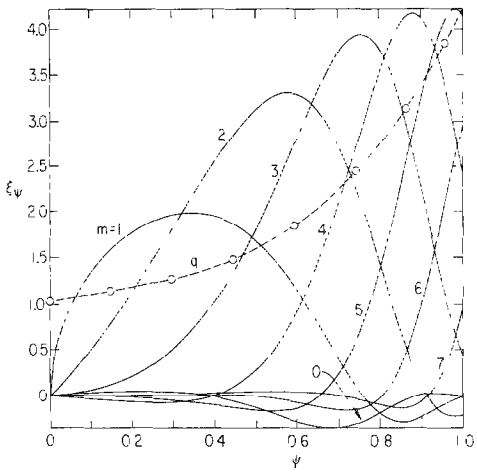

FIG. 5. The poloidal components of the converged $n=1$ free boundary external kink mode eigenfunction ξ_ψ versus ψ. It is computed with an equal arc length θ-coordinate for a bean-shaped equilibrium with the parameters $\tilde{X}_0=2.71$, $d/2a=0.3035$, $b/a=1.7385$, $R/a=3.449$, $\langle\beta\rangle_{a\iota}=8.75\%$, $q(0)=1.03$, $q(1)=4.2$, $P_0=0.109$. The eigenvalue is $\gamma^2=3.5$ and the q-profile is also shown.

ponents of converged eigenfunction ξ_ψ for the equal arc length θ-coordinate and the PEST θ-coordinate, respectively. The plasma flow pattern on the $\phi=0$ plane is shown in Fig. 7 where large flow is clearly seen on the outside of the torus. Thus, the external kink can be effectively stabilized by placing a metal plate on the outside of the torus to stop or reduce the flow.

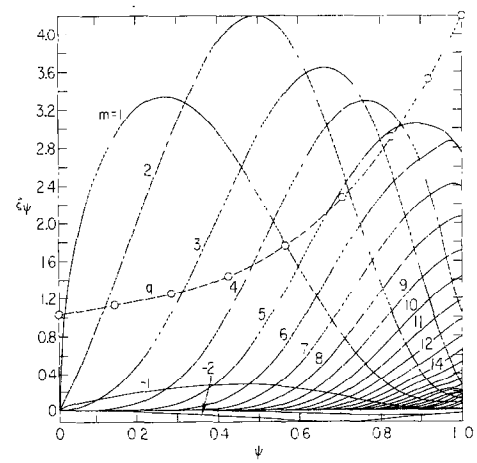

FIG. 6. The poloidal components of the converged $n=1$ free boundary external kink mode eigenfunction ξ_ψ versus ψ with PEST θ-coordinate for the same bean-shaped equilibrium as in Fig 5.

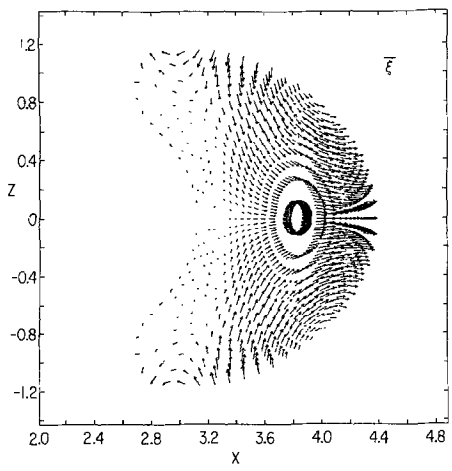

FIG. 7. The projection of the plasma flow on the $\phi = 0$ plane is shown for the $n = 1$ free boundary external kink mode for the same case as in Fig. 5.

VI.b. *Internal Kink Modes*

The $n = 1$ ideal MHD internal kink is usually unstable in tokamak plasmas when [illegible] growth rate of this mode is typically a factor of ε^2 smaller than the more dangerous external kinks, where ε is the inverse aspect ratio. Its eigenfunction ξ_ψ is localized inside the $q = 1$ surface and decreases rapidly to zero outside. Because of the small growth rate and the need to resolve the $q \leqslant 1$ region accurately, studying this mode provides a challenge for testing a stability code. A specially tailored r-grid with grid packing near the $q = 1$ surface has been used to obtain accurate results. The tailored r-grid usually produces faster convergence than the tailored ψ-grid when the $q = 1$ surface is closer to the magnetic axis. This is because the r-grid weights the region near the magnetic axis more heavily than the ψ-grid. In general, accurate representation of the eigenfunction near the rational surfaces is also of critical importance to boundary layer treatment of nonideal instabilities, such as the resistive tearing modes, kinetic fishbone modes, etc.

We consider a PDX-type equilibrium with circular plasma surface computed from a flux equilibrium code with the profiles $P(y) = P_0(1 - y^2)^2$, $q(y) = q(0) + y\{q(1) - q(0) + (y - 1)[q'(1) - q(1) + q(0)](1 - y_s)/(y - y_s)\}$, where $y_s = [q'(1) - q(1) + q(0)]/\{q'(0) + q'(1) - 2[q(1) - q(0)]\}$, $y = \psi/\Delta\psi$. The parameters are $\Delta\psi = 0.0609$, $\langle\beta\rangle_{av} = 1.277\%$, $R = 1.43$, $R/a = 3.4$, $P_0 = 0.02456$, $q(0) = 0.8$, $q(1) = 2.85$, $q'(0) = 13.857$, and $q'(1) = 106.88$. For the $n = 1$ fixed boundary mode the eigenvalue is $\gamma^2 = 2.306 \times 10^{-3}$ and the eigenfunction ξ_ψ versus r is shown in Fig. 8. The q-profile is also shown in Fig. 8. The plasma flow pattern at $\phi = 0$, shown in Fig. 9, clearly indicates large flow at the $q = 1$ surface with the dominant

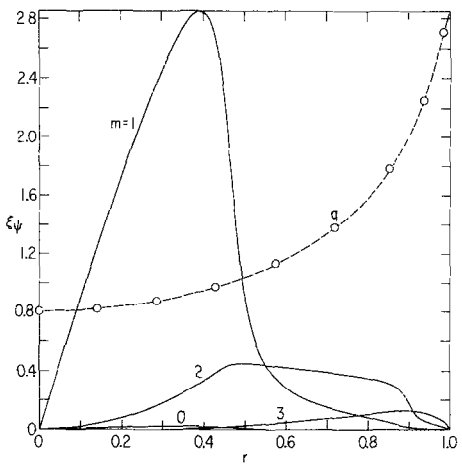

FIG. 8. The poloidal components of the $n=1$ fixed boundary internal kink mode eigenfunction ξ_ψ versus r. The equilibrium has a circular plasma surface with $R=1.43$, $R/a=3.4$, $q(0)=0.8$, $q(1)=2.85$, $P_0=0.02456$. $\langle\beta\rangle_{av}=1.277\%$. The eigenvalue is $\gamma^2=2.306\times10^{-3}$ and the q-profile is also shown.

$m=1$ component. The computation was carried out with the equal arc-length θ coordinate, and the dominant poloidal harmonics are $1\leqslant m\leqslant 3$. Because of the relatively high growth rate, we do not have to pack many grid points near the $q=1$ and $q=2$ surfaces. However, for smaller growth rates the eigenfunction exhibits a sharp gradient, and local packing of more grid points near singular surfaces may be necessary.

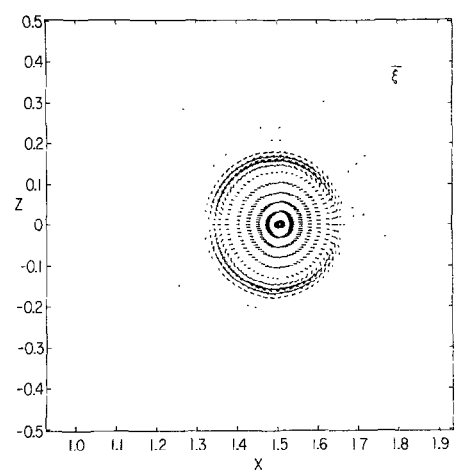

FIG. 9. The projection of the displacement vector ξ onto the $\phi=0$ plane for the $n=1$ fixed boundary internal kink mode shown in Fig. 8.

VI.c. *Toroidicity-Induced Alfvén Waves*

Recent studies of the stable shear Alfvén spectrum for toroidal plasmas using the ideal MHD model have led to the discovery of the discrete toroidicity-induced Alfvén waves [9]. The toroidal coupling effects due to a nonuniform magnetic field over a magnetic surface can cause interactions among the neighboring poloidal harmonics and can break up the shear Alfvén continuous spectrum resulting in continuum gaps. In addition, discrete, global, toroidicity-induced eigenmodes were found with frequencies inside the continuum gaps. The existence of these toroidicity-induced shear Alfvén eigenmodes suggests a new efficient Alfvén wave heating scheme. In addition, instabilities can be excited by tapping the free energy of energetic particles associated with the plasma inhomogeneities through wave-particle resonances. Fig. 10 shows the ploidal harmonics of the $n=1$ fixed boundary eigenfunction ξ_ψ versus ψ for a low-β, circular numerical equilibrium. The numerical equilibrium has the same $P(\psi)$ and $q(\psi)$ functional forms as in Fig. 8 but with the parameters: $P_0=4.55\times10^{-4}$, $R/A=4$, $R=1$, $q(0)=1.05$, $q(1)=2.3$, $q'(0)=36.12$, $q'(1)=140$, $\Delta\psi=0.020768$, and $\langle\beta\rangle_{\text{av}}=0.0407\%$. The eigenfrequency of this fixed boundary $n=1$ mode is $\omega^2=0.5$. The q-profile is also shown in Fig. 10. It is clear from Fig. 10 that primarily $m=1$ and 2 harmonics dominate around the $q=1.5$ surface with a small coupling to $m=3$ harmonics toward the plasma surface. Projection of the displacement vector ξ onto the $\phi=0$ plane is shown in Fig. 11, where the plasma vortices corresponding to $m=1$ and 2 harmonics are clearly seen. Note that, due to the regular mode structure and the existence of the continuum gap, the numerical computation is rather easy.

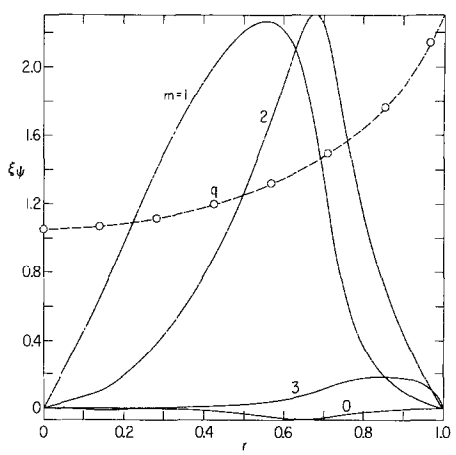

FIG. 10. The poloidal harmonics of the $n=1$ fixed boundary toroidicity-induced shear Alfvén eigenmode, ξ_ψ, versus r for a low β circular equilibrium with the parameters: $R=1$, $R/a=4$, $q(0)=1.03$, $q(1)=2.3$, $P_0=4.55\times10^{-4}$, and $\langle\beta\rangle_{\text{av}}=0.0407\%$. The q-profile is also shown and the eigenvalue is $\omega^2=0.5$.

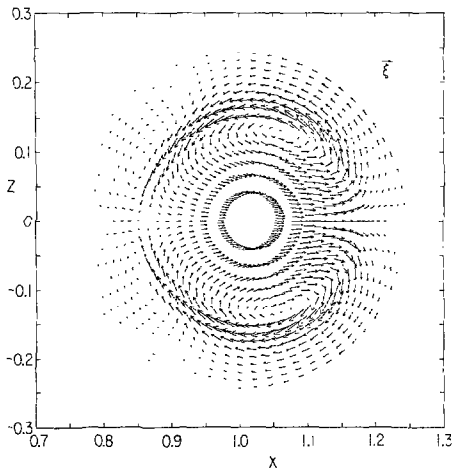

FIG. 11. The projection of the displacement vector ξ on to the $\phi = 0$ plane for the $n = 1$ fixed boundary toroidicity-induced shear Alfvén eigenmode as shown in Fig. 10.

VI.d. *Shear Alfvén Continuum Mode*

The continuum spectrum is due to the singular nature of the ideal MHD model [13] and is a result of the noninvertibility [9, 14] of the surface operator E in Eq. (25). The continuum eigenfunctions have singular behavior somewhere inside the plasma. At the resonance surface ψ_0, the eigenfunction can behave [21] locally as $[C_1 \ln(\psi - \psi_0) + C_2]$. The constant C_2 can have an arbitrary finite discontinuity.

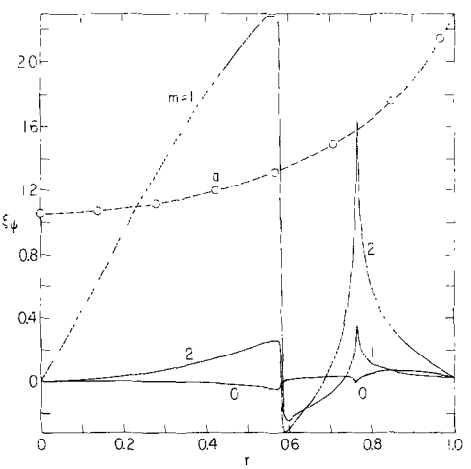

FIG. 12. The poloidal harmonics of the $n = 1$ fixed boundary continuum mode ξ_ψ versus r for the same equilibrium as in Fig. 10. The eigenvalue is $\omega^2 = 0.302$ and the q-profile is also shown.

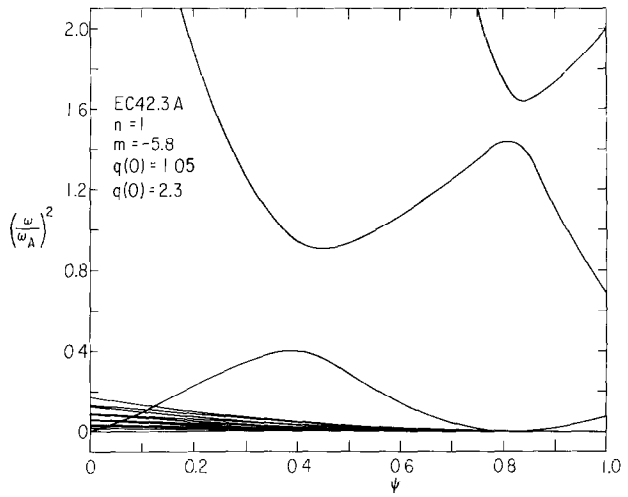

FIG. 13. The $n = 1$ continuous spectrum for the same equilibrium as in Fig. 12.

which provides the possibility of satisfying the boundary conditions for a continuous set of eigenvalues and leads to a continuous spectrum. In numerical calculations the continuous spectrum is approximated by a dense set of discrete eigenvalues with the number of discrete eigenvalues proportional to the number of grid points. These numerical discrete eigenvalues are only the approximate solutions of Eq. (30) and we do not encounter difficulties in inverting the surface operator E in Eq. (25). Figure 12 shows the eigenfunction of the $n = 1$ fixed boundary continuum mode with frequency $\omega^2 = 0.302$ for the same equilibrium as in Fig. 10. Figure 13 shows the approximate continuous spectrum [9] from the solutions of Eq. (30) for the same numerical grid points as used in Fig. 12. Comparing Fig. 12 with Fig. 13, our numerical solution ξ_ψ correctly shows the $\ln|\psi - \psi_0|$ behavior near the singular surface of the $m = 2$ mode and a jump discontinuity near the singular surface of the $m = 1$ mode. These singular surfaces are the locations of the singularities of the surface operator E in Eq. (25) for the continuum $\omega^2 = 0.302$.

VII. CONCLUSION

In this paper we have presented a nonvariational ideal MHD stability code (NOVA) which represents an accurate and efficient approach for determining the ideal MHD spectrum and stability of axisymmetric toroidal confinement systems. In a general flux coordinate system the code makes use of the cubic B-spline finite elements in the minor radius direction and Fourier expansion in the poloidal direction. The ideal MHD eigenmode equations are reduced to a set of coupled second order differential equations in the minor radius coordinate. With the cubic B-spline

finite elements, we are reduced to solving a matrix equation with nontrivial solutions. In comparison with the existing variational codes [1–6], the NOVA code can produce more accurate results with less computational efforts. The code is fast and efficient on a CRAY-1 computer so that it is written in the interactive mode which can provide more flexible usages. The code has also been applied to several typical problems to illustrate the convergence properties with diiferent coordinate systems.

The improved efficiency over the previous variational codes may allow for an examination of the stability of fully three-dimensional magnetic confinement devices, such as stellarators. Finally, since the numerical procedure does not rely on the variational energy principles, this successful nonvariational approach can be easily extended to other physical problems where the eigenmode equations are non-Hermitian [22].

ACKNOWLEDGMENTS

The authors would like to thank Dr. D. Monticello for useful discussions on the flux equilibrium and mapping codes. This work is supported by U.S. DOE Contract DE-AC02-76-CHO-3073.

REFERENCES

1. R. C. GRIMM, J. M. GREENE, AND J. L. JOHNSON, *Methods in Computational Phys.*, edited by J. Killeen (Academic Press, New York, 1976), Vol. 16, p. 253.
2. R. GRUBER, F. TROYON, D. BERGER, L. C. BERNARD, S. ROUSSET, R. SHREIBER, W. KERNER, W. SCHNEIDER, AND K. V. ROBERTS, *Comput. Phys. Comm.* **21**, 323 (1981).
3. W. KERNER, *Nucl. Fusion* **16**, 643 (1976).
4. L. C. BERNARD, F. J. HELTON, AND R. W. MOORE, *Comput. Phys. Comm.* **24**, 377 (1981).
5. L. M. DEGTYAREV, V. V. DROZDOV, A. A. MARTYNOV, AND S. YU. MEDVEDEV, in *Proceedings of International Conference on Plasma Physics, Lausanne, Switzerland, 1984*, edited by M. Q. Tran, *et al.* (École Polytechnique, Fédérale de Lausanne, 1984), Vol. I. pp. 157–175.
6. R. C. GRIMM, R. L. DEWAR, AND J. MANICKAM, *J. Comput. Phys.* **49**, 94 (1983).
7. I. B. BERNSTEIN, E. A. FRIEMAN, M. D. KRUSKAL, AND R. M. KULSRUD, *Proc. Roy. Soc., Ser. A* **244**, 17 (1958).
8. K. S. KUNZ, *Numerical Analysis* (McGraw-Hill, New York, 1957), p. 100; C. DEBOOR, *J. Approx. Theory* **6**, 50 (1972).
9. C. Z. CHENG AND M. S. CHANCE, *Phys. Fluids* **29**, 3695 (1986).
10. L. S. SOLOVÉV, *Sov. Phys. JETP* **26**, 400 (1968).
11. M. S. CHANCE, J. M. GREENE, R. C. GRIMM, J. L. JOHNSON, J. MANICKAM, W. KERNER, D. BERGER, L. C. BERNARD, R. GRUBER, AND F. TROYON, *J. Comput. Phys.* **28**, 1 (1978).
12. A. H. BOOZER, *Phys. Fluids* **23**, 904 (1980); **26**, 496 (1985); R. B. WHITE AND M. S. CHANCE, *Phys. Fluids* **27**, 2455 (1984).
13. Z. SEDLACEK, *J. Plasma Phys.* **5**, 239 (1971).
14. E. HAMEIRI, *Commun. Pure Appl. Math.* **38**, 43 (1985); J. P. GOEDBLOED, *Phys. Fluids* **18**, 1250 (1975).
15. K. APPERT, R. GRUBER, AND J. VACLAVIK, *Phys. Fluids* **17**, 1471 (1974).
16. J. C. WILEY, The University of Texas Report FRCR No. 131, 1977 (unpublished).

17. M. S. CHANCE, R. L. DEWAR, A. M. M. TODD, J. MANICKAM, R. C. GRIMM, J. M. GREENE, AND J. L. JOHNSON, in *Proceedings of the 8th International Conference on Numerical Simulation of Plasmas, Monterey, CA June 28–30, 1978*, PC-5; M. S. CHANCE AND C. Z. CHENG, in *Proceeding of the 11th International Conference on Numerical Simulation of Plasmas, Montreal, Canada, June 25–27, 1985*, 2.B.05.
18. R. LÜST AND E. MARTENSEN, *Z. Naturforsch. A* **15**, 706 (1960).
19. M. S. CHANCE, S. J. JARDIN, AND T. H. STIX, *Phys. Rev. Lett.* **51**, 1963 (1983).
20. W. KERNER, R. GRUBER, AND F. TROYON, *Phys. Rev. Lett.* **44**, 536 (1980).
21. R. L. DEWAR, J. M. GREENE, R. C. GRIMM, AND J. L. JOHNSON, *J. Comput. Phys.* **18** 132 (1975).
22. W. KERNER, *Comput. Phys. Comm.* **36**, 225 (1985).